A simplified Suomi NPP VIIRS dust detection algorithm

Yikun Yang [a], Lin Sun [a,*], Jinshan Zhu [a], Jing Wei [a,b], Qinghua Su [a,c], Wenxiao Sun [a], Fangwei Liu [a], Meiyan Shu [a]

[a] College of Geomatics, Shandong University of Science and Technology, Qingdao 266590, China
[b] Institute of Space and Earth Information Science, The Chinese University of Hong Kong, Shatin 999077, Hong Kong
[c] School of Geography and Tourism, Qufu Normal University, Qufu 273165, China

ARTICLE INFO

ABSTRACT

Due to the complex characteristics of dust and sparse ground-based monitoring stations, dust monitoring is facing severe challenges, especially in dust storm-prone areas. Aim at constructing a high-precision dust storm detection model, a pixel database, consisted of dusts over a variety of typical feature types such as cloud, vegetation, Gobi and ice/snow, was constructed, and their distributions of reflectance and Brightness Temperatures (BT) were analysed, based on which, a new Simplified Dust Detection Algorithm (SDDA) for the Suomi National Polar-Orbiting Partnership Visible infrared Imaging Radiometer (NPP VIIRS) is proposed. NPP VIIRS images covering the northern China and Mongolian regions, where features serious dust storms, were selected to perform the dust detection experiments. The monitoring results were compared with the true colour composite images, and results showed that most of the dust areas can be accurately detected, except for fragmented thin dusts over bright surfaces. The dust ground-based measurements obtained from the Meteorological Information Comprehensive Analysis and Process System (MICAPS) and the Ozone Monitoring Instrument Aerosol Index (OMI AI) products were selected for comparison purposes. Results showed that the dust monitoring results agreed well in the spatial distribution with OMI AI dust products and the MICAPS ground-measured data with an average high accuracy of 83.10%. The SDDA is relatively robust and can realize automatic monitoring for dust storms.

1. Introduction

Desertification is becoming increasingly serious under the background of global warming, especially in arid and semi-arid areas where dust storms occur more frequently. Dust can directly affect the earth's radiation balance by absorbing and scattering solar radiation and emitting long-wave radiation (Tegen, 2003; Zhao et al., 2013; Bilal et al., 2017; Sun et al., 2015; Wei and Sun, 2017), and it can indirectly affect the Earth's revenue and energy balance by acting as cloud condensation nuclei and altering the lifetime of clouds (Albrecht, 1989; Huang et al., 2006; Bilal et al., 2013; Hillger et al., 2014). In addition, long-distance dust transport will seriously affect human life along the transport route, resulting in huge economic losses.

In recent years, with the rapid development of remote sensing technologies, remote sensing images that have wide spatial coverages and multiple detection channels have come to play important roles in dust detection. Dust has a strong absorption of visible light and near infrared wavelengths; and can weaken amount of the sun's radiance that reaches the ground. Dust can also absorb long wave radiation from the ground

and emit long wave radiation. Thus, the above unique and typical optical properties can be used in dust detection. Many satellites have been applied to dust storm detection, such as the Advanced Very High Resolution Radiometer (AVHRR) (Amato et al., 2006; Janugani et al., 2008), Moderate Resolution Imaging Spectroradiometer (MODIS) (Gharai et al., 2013; Cao et al., 2015), Chinese FengYun series (FY) (Zhou et al., 2007; Hu et al., 2008), Total Ozone Mapping Spectrometer (TOMS) (Kaskaoutis et al., 2008; Awad et al., 2016) and Ozone Monitoring Instrument (OMI) (Kaskaoutis et al., 2010; Jafari and Malekian, 2015; Madhavan et al., 2017).

Globe ecological issues have attracted increasing attention from the public with the development of the society, and to date, a great deal of systematic research has been done on remote sensing dust detection (Claquin et al., 1999; Zheng et al., 2001; Miller, 2003; Amato et al., 2006; Hu et al., 2008; Zhao et al., 2010; Xu et al., 2011, 2016; Borgne et al., 2013; Di et al., 2016). Ackerman used the radiative transfer model to simulate the radiation characteristics of thermal infrared channels (8.5 μm, 11 μm and 12 μm) and realized dust detection with AVHRR data under a clear sky by using the Brightness Temperature Difference (BTD)

of thermal infrared channels (Ackerman, 1997). Hao and Qu calculated the Thermal infrared Dust Index (TDI) by studying the relationships of brightness temperature and Aerosol Optical Depth (AOD) of MODIS channels 20, 30, 31, and 32, which was then adopted from strong sand storms that occurred over the Atlantic Ocean during 2004–2006. The results showed that the MODIS AOD had high consistency with TDI and can be used for dust intensity monitoring (Hao and Qu, 2007). Borgne et al. simulated the influence of dust aerosols in different altitudes and concentrations to the brightness temperature of intermediate and thermal infrared channels, and modified the Saharan Dust Index (SDI) to monitor dust using Suomi NPP VIIRS (Visible Infrared Imaging Radiometer Suite) data at night (Borgne et al., 2013). Dust detection accuracy is influenced by many factors, such as underlying surface type, dust intensity, altitude of the dust layer and cloud type (Jafari and Malekian, 2015). In addition, to improve the detection accuracy and decrease the impact of clouds and surface inhomogeneity, the dust storm detection algorithms, which utilize visible, near infrared (NIR) and thermal infrared (TIR) channels, are also widely applied. Miller uses visible and near infrared wavelengths to provide additional colour information for dust monitoring in the thermal infrared channel, enabling sand and dust monitoring over both land and ocean (Miller, 2003). Based on the spectral and radiative physical properties of mid-infrared and thermal infrared channels, Hu et al. (2008) proposed a dust retrieval algorithm using the BTD, Infrared Difference Dust Index (IDDI) and the ratio of middle infrared reflectance to visible reflectance. Correlation analyses were performed between dust monitoring results, PM_{10}, horizontal visibility and AOD, and the results showed that the algorithm can realize automatic dust detection with high accuracy and a low false alarm rate (Hu et al., 2008). Zhao et al. realized dust and smoke monitoring over ocean and land by using visible, NIR, Mid-Infra-Red (MIR) and TIR channels, which can be used for global thick dust and heavy smoke monitoring, except in ice/snow areas (Zhao et al., 2010). Samadi and Boloorani established training samples of dust, cloud pixels and various surface types and performed spectral analyses on all channels of MODIS, and a Global Dust Detection Index (GDDI) was developed, which can be applied for the effective extraction of dust ranging over ocean and land (Samadi and Boloorani, 2014). Di et al. analysed BTDs, aerosol properties of dust and other surface features in visible, NIR and thermal infrared channels and proposed the Enhanced Dust Index (EDI); the dust

monitoring results showed high consistency with surface visibility data ($R^2 = 0.78$) (Di et al., 2016).

On the basis of previous research results, a pixel database including a variety of typical feature types, such as dust over different surface types, cloud, vegetation, Gobi, and ice/snow were collected, and the distributions of the top-of-atmosphere (TOA) reflectance and brightness temperatures were analysed; based on which a Simplified Dust Detection Algorithm (SDDA) was generated. This method is based on a prior pixel database, which is constructed by selecting dust pixel values over different land use types for different specific sensor channels. It can reduce the effects of changes in sensor characteristics on the monitoring results. Multi-temporal Suomi NPP VIIRS images containing dust storms were collected and applied to detection experiments with the proposed algorithm. In addition, the Meteorological Information Comprehensive Analysis and Process System (MICAPS) dust ground-measured data and OMI Aerosol Index (AI) products, which can well describe the distribution of dust storms, were selected for validation and comparison.

2. Study area and data source

2.1. Study area

In this paper, the northern China and Mongolian regions (32°E ~ 47°E, 74°N ~ 123°N) were selected as the study area (Fig. 1). Due to the influence of a temperate continental climate, these areas are controlled by continental air masses year-round and are dominated by dry weather, especially in winter and spring. At the same time, the Eurasian continent formed a high-pressure area in spring and winter that is influenced by the monsoon, and China's coastal areas formed a low-pressure area affected by ocean water, leading to strong winds and dust storms when the atmosphere was transported from inland to coastal areas, causing huge economic losses.

2.2. Data source

2.2.1. VIIRS data

VIIRS is the expansion and improvement of the AVHRR and MODIS sensors on board the Suomi NPP satellite. It is a geosynchronous orbit satellite that transits at local time 13:30 every day. It captures data in 22
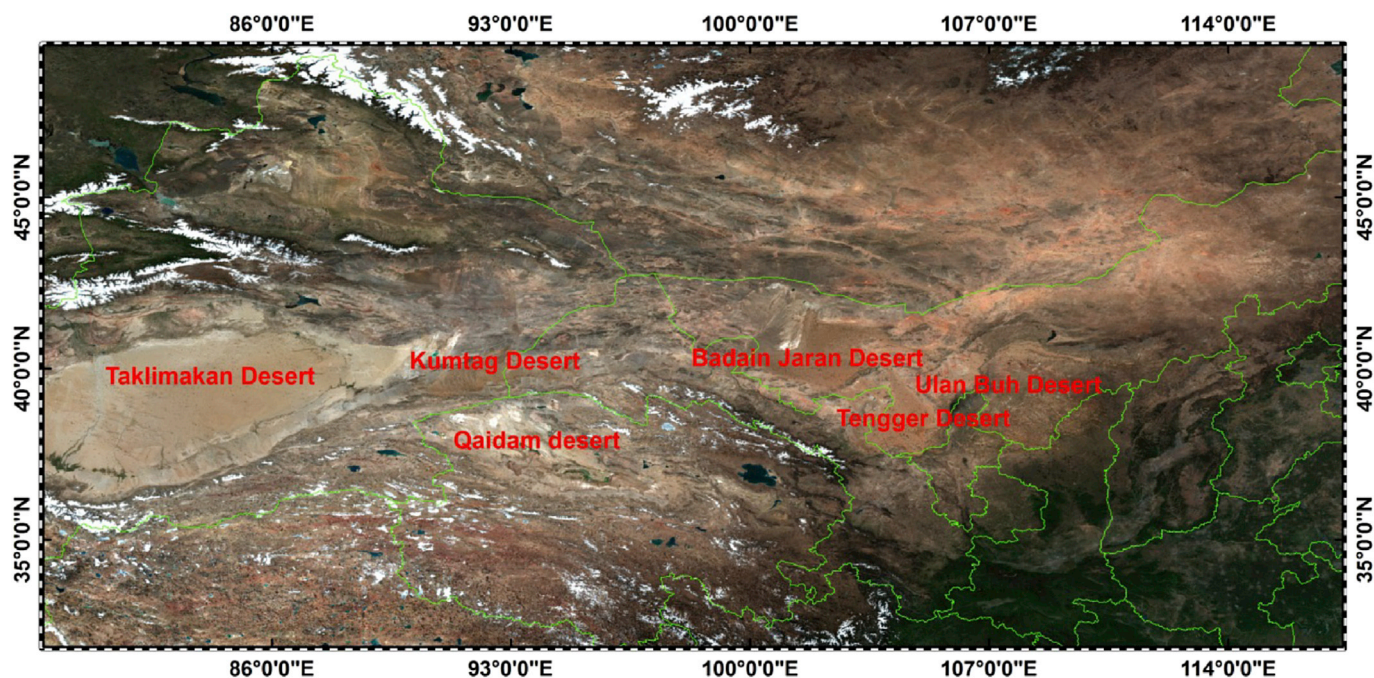

Fig. 1. Geographical location of the study area.

spectral channels that range in wavelength from 0.402 μm to 12.488 μm and have varying spatial resolutions, including five high-resolution I-channels (375 m), sixteen medium-resolution M-channels (750 m) and one panchromatic Day/Night channel (750 m). The M-channels cover eleven Reflectance Solar Channels (RSB) and five Thermal Emissive Channels (TEB) (Hillger et al., 2014), and detailed parameters are shown in Table 1. The reflectance of the visible and NIR channels and the brightness temperature of the thermal infrared channels have been widely used in dust storm monitoring (Chen et al., 2014).

2.2.2. MICAPS data

MICAPS is a satellite communication and database supported human-computer interaction system that is used for the production of weather forecasting. Its main function is to display graphs and images of meteorological data and to edit and process meteorological graphs. It can also provide weather forecasting working platforms in the medium-term, short-term and current-time. Ground observation data, aerological sounding data, satellite cloud image data, and so on, a total of 19 kinds of data included in the MICAPS. Table 2 shows the dust information and the correspond code in MICAPS.

2.2.3. OMI AI products

Aura, the third satellite of the Earth Observation System (EOS), was successfully launched on 15 July, 2004. Onboard the Aura, the OMI possesses the Global Ozone Monitoring Experiment (GOME), the SCanning Imaging Absorption spectroMeter for Atmospheric CHartographY (SCIAMACHY) and TOMS, observing the earth with a resolution of 13 km × 24 km on a global scale (daily). OMI wavelengths range from 270 nm to 500 nm, containing two ultraviolet (UV) channels UV1 (270–310 nm), UV2 (310–365 nm) and a visible channel VIS (365–500 nm) (Levelt et al., 2006).

Compared with visible channels, the surface reflectance of the UV channel is low, except for ice/snow, and clouds. The reflectance difference is less in UV, and the radiation energy received by the sensor is mainly from atmospheric scattering; the mutual effects of atmospheric particle scattering and aerosol make it possible to estimate the atmospheric aerosol absorption in a UV channel (Badarinath et al., 2008). The AI is calculated as the residual between the measured and calculated radiance using the Lambert Equivalent Reflectivity (LER) (Kaskaoutis et al., 2010). Before using the OMI near-UV aerosol algorithm (OMAERUV), the first step is to calculate the LER R_{388}^* at 388 nm by assuming that the atmospheric scattering is pure Rayleigh and that the atmosphere is bounded by an opaque Lambertian reflector of reflectance R_{388}^* (Torres et al., 2007). The LER at 354 nm (R_{354}^*) is calculated using R_{388}^*:

$$AI = -100 \, log_{10} \left[\frac{I_{354}^{obs}}{I_{354}^{calc}\left(R_{354}^*\right)} \right] \tag{1}$$

Table 1
NPP VIIRS image M channels.

Channels	Wavelength Range (μm)	Wavelength Center (μm)	Resolution (m)
M1	0.402–0.422	0.412	750
M2	0.436–0.454	0.445	750
M3	0.478–0.498	0.488	750
M4	0.545–0.565	0.555	750
M5	0.662–0.682	0.672	750
M7	0.846–0.885	0.865	750
M8	1.23–1.25	1.24	750
M10	1.58–1.64	1.61	750
M11	2.225–2.275	2.25	750
M12	3.66–3.84	3.7	750
M13	3.973–4.128	4.05	750
M14	8.4–8.7	8.55	750
M15	10.263–11.263	10.763	750
M16	11.538–12.488	12.013	750

Table 2
MICAPS codes of dust weather.

Code	Code Meaning	Code	Code Meaning
6	Dust in Suspension	7	Floating dust
8	dust devil	9	Dust storm
30	Mild dust storm weakened in the past hour	31	Mild dust storm
32	Mild dust storm enhanced in the past hour	33	Strong dust storm weakened in the past hour
34	Strong dust storm	35	Strong dust storm enhanced in the past hour

where I_{354}^{obs} is the radiation recorded by a sensor and I_{354}^{calc} is the calculated LER.

The AI is a measure of the Rayleigh-scattered radiance from aerosol absorption. When a strong absorptive aerosol is present, the OMI-AI value of a dust storm is greater than 0 and increases with an increase of in dust storm concentration. The AI of a cloud coverage area is approximately zero, whereas the non-absorptive aerosol AI is negative. As an improvement of TOMS AI, AI has been widely used in atmospheric particle detection (Li et al., 2014), and its products are generally used to validate the dust detection results (Sang et al., 2014). Kaskaoutis analysed dust intensity in 2008, and the results indicated that both OMI AI and TOMS AI can accurately describe the dust storm areas (Kaskaoutis et al., 2008). In addition, he analysed the AI spatial, seasonal and inter-annual variations between 2004 and 2008 and found that the AI was sensitive to UV-absorptive dust aerosols (Kaskaoutis et al., 2010). Jafari and Malekian compared and evaluated the performance of five dust detection algorithms using MODIS Deep Blue (DB) AOD and OMI AI products (Jafari and Malekian, 2015).

3. Dust monitoring principles and methods

3.1. Dust radiation characteristics

The World Meteorological Organization (WMO) divides dust storms into four grades, according to intensity: dust-in-suspension (visibility: > 10 km), blowing dust (visibility: 1–10 km), dust storm (visibility: 200–1000 m) and severe dust storm (visibility: < 200 m) (WMO, 2005). From dust-in-suspension to dust storm, the dust particle radius ranges from 0.01 μm to 100 μm, whereas dust storms are mainly composed of dust particles with radii of more than 5 μm (Zheng et al., 2001). In far-IR channels, dust particles emit long-wave radiation by absorbing solar short-wave radiation, and the emission can be weakened with increasing wavelength. Due to similar radiation characteristics of dust storms with land use types and the effects of several factors such as particle size, shape and texture, dust storms can rarely be accurately identified by using a single channel. According to previous research, dust has lower reflectance in the blue channel compared with other surface features (e.g., water, vegetation, cloud), whereas it has higher reflectance in the infrared channel; thus, dust detection can be comprehensively performed using both visible and near-infrared channels (Wallace, 2006). In mid-wave infrared wavelengths, the radiation energy received by a sensor includes both the back scattering of solar radiation reflected by dust and the long-wave radiation emitted by it. With an increase in wavelength, the reflecting solar radiation ability of dust can be reduced, so dust identification can be realized by using the BTDs between the short-wave infrared and the thermal infrared channels (Ackerman, 1989). Ackerman found the BTDs in the thermal infrared channel (8–12 μm): water vapour absorption at 12 μm and 8.5 μm were more obvious than at 11 μm under clear sky. When dust weather occurs, the extinction effect at 11 μm is much larger than those at 12 μm and 8.5 μm; thus, dust storm monitoring can be performed according to the brightness differences at 8.5 μm, 11 μm and 12 μm (Ackerman, 1997).

3.2. Dust storm detection method

The northern China and Mongolian regions feature complex surface types, including desert, Gobi, bright surface, vegetation and snow-covered areas. To analyse the reflectance characteristics of different surface features in the NPP VIIRS visible and near-infrared channels as well as the brightness temperature characteristics of the middle- and far-infrared channels, several surface types were adopted in this study as training samples, including thick dust, thin dust, vegetation, thin cloud, thick cloud and bare land. In addition, training samples were selected from pixels with different time phases and regions in decrease random error and increase the universality of the dust detection algorithm. The mean reflectance of samples as radiation characteristics was calculated, Fig. 2 shows the radiation differences of surface features in VIIRS channels, except for M6 and M9, which are affected by sensor Rotating Telescope Assembly (RTA) mirror surface contamination (Moeller, 2012) and the strong absorption by water vapour, respectively.

3.2.1. Cloud/ice/snow identification

Thick clouds and snow have high reflectance in visible channels (Fig. 2-a) and low brightness temperatures (Fig. 2-b) compared with other surface features. The TOA reflectance of dust lies between those of dark surfaces and bright surfaces. In MIR channels, dust can not only reflect solar radiation but also emit long-wave radiation, leading to high brightness temperatures. Therefore, ice/snow, thick clouds and dust can be separated using the visible and brightness temperature channels. In this study, to intuitively analyse the differences of clouds and ice/snow and to realize dust information extraction, we randomly selected reflectances of cloud, ice/snow and dust in blue channel and their brightness temperatures in the mid-infrared channel to draw the scatter plot (Fig. 3). Moreover, the variances of sample points were calculated to show standard deviations in the blue (M3) and NIR (M12) channels (Fig. 4).

As shown in Fig. 3, the reflectance and brightness temperature of ice/snow area differ greatly and are influenced by melting degree, thus showing a discrete two-dimensional space distribution. Due to the impact of the surface feature types, the radiation characteristics of thin cloud fluctuate wildly, especially over Gobi or desert, which leads to overlap in the scatter plot. Overall, cloud and ice/snow areas have lower brightness temperature than do dust area in MIR channels, with higher reflectance in the blue channel; thus, cloud and ice/snow can be removed based on a simple threshold algorithm by comprehensively using the blue (M3) and MIR (M12) channels.

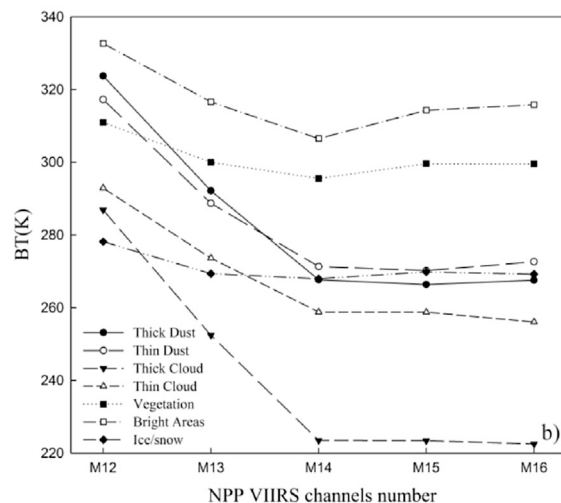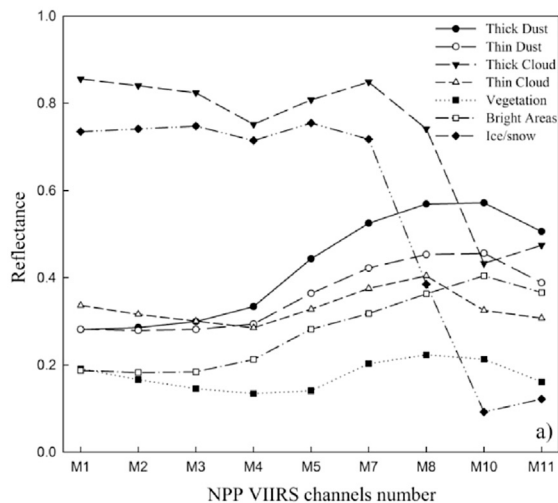In this study, we calculated the mean reflectances of thick/thin dust,

Fig. 3. Scatter plot of brightness temperature (M12) versus reflectance (M3) for thick dust (Black), thin dust (Red), thick cloud (Green), thin cloud (Yellow) and ice/snow (Blue). (For interpretation of the references to colour in this figure legend, the reader is referred to the web version of this article.)

thick/thin cloud and ice/snow and selected the deviation as the random error (Fig. 4). In thin cloud areas, the radiation energy received by the sensor is the sum of land surface reflection and thin cloud reflection. Therefore, the radiation characteristics of thin cloud areas are difficult to determine, because the radiation error distribution is large and is similar to that of ice/snow. Most of the thick clouds and parts of thin clouds and ice/sow surfaces can be identified and removed as follows:

$$\rho_3^* \geq 0.44 \ or \ BT_{12} \leq 300 \tag{2}$$

where ρ_3^* represents the top-of-atmosphere reflectance of channel 3 and BT_{12} represents the brightness temperature of channel 12 for VIIRS data.

3.2.2. Bright surface removal

Influenced by climate conditions, dust weather generally occurs in arid and semi-arid areas, where the land surface is barren and desertification is serious. At the same time, dust storms usually occur in dry seasons, when the vegetation is in the wilting period. In the visible

Fig. 2. The spectral curves of the typical surfaces in the pixel database, except for channels 6 and 9. a) The top-of- atmosphere reflectance of typical surfaces in visible and near infrared channels. b) The brightness temperature of typical surfaces in the middle-infrared and thermal-infrared channels (from 3.6 μm to 12 μm).
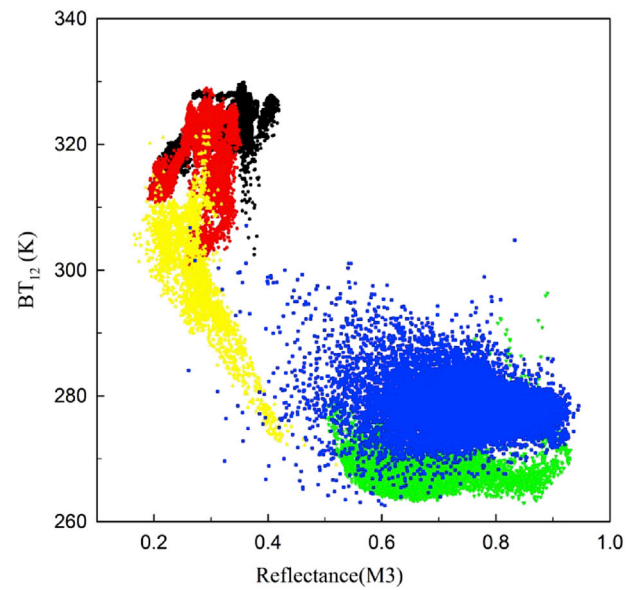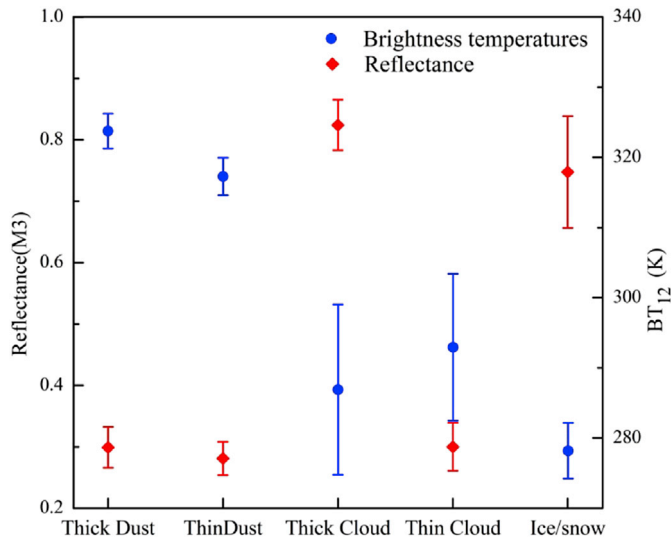
Fig. 4. One standard deviation away from the means of thick dust, thin dust, thick cloud, thin cloud and ice/snow. The diamonds and circles represent the reflectance of the M3 channel and brightness temperatures of the M12 channel, respectively.

Fig. 5. One standard deviation away from the means of the brightness temperature difference in VIIRS channel 14 and channel 15. The horizontal and vertical axes represent the objects in the pixel database and the difference of brightness temperature, respectively.

channels, the reflectance of bright surfaces is very similar to that of dust, especially in a region with thin dust (Fig. 2a). The sample points have large standard deviations, indicating wide ranges of TOA reflectance for bright surfaces. Therefore, it is difficult to separate the dust and bright surfaces from the visible channels. For the Badain Jaran Desert in the west of Inner Mongolia, the deserts appears as red in the true colour composite images because the dust particles are rich in minerals. The reflectance is relatively lower compared with the dust, Gobi desert and desert, which can be used to distinguish desert from dust because the reflectance in the visible channel is lower than a certain threshold. The brightness temperature of the bright surface area at 8.5 μm (M14) is particularly lower compared to that of 10.763 μm (M15) (Fig. 2b). To more clearly and visually analyse the differences between the bright surfaces and other objects in channels 14 and 15 of VIIRS data, the BTDs and standard deviations of all objects in the pixel database were calculated (Fig. 5).

Compared with other objects in the pixel database, the bright surfaces show the lowest mean BTD at approximately −8 K. The water vapour absorption in the 8.5 μm (M14) channel is greater than that in the 10.763 μm (M15) channel and as the water vapour content increases, the difference becomes larger (Ackerman, 1997). In contrast, the BTD between 8.5 μm (M14) and 10.763 μm (M15) is known to show positive values for dust due to the extinction effect of dust particles (Ackerman, 1997; Chen et al., 2014). Thus, the bright surface can be removed as follows:

$$BT_{14} - BT_{15} \leq -5.0 \tag{3}$$

where BT_i represents the brightness temperatures of channels i for VIIRS data.

3.2.3. Dark surface removal

The TOA reflectance of dust storms shows similar change trends as does vegetation, especially in the spring and winter seasons, when the vegetation exhibits dark tones similar to dust storms in the true colour images. According to the characteristics of the infrared channels, the dust can both reflect the solar radiation and emit the long-wave radiation in mid-infrared channels. In addition, in thermal infrared channels, the long-wave radiation capability of the dust emission decreases with an increase in wavelength. The absorption and decrease the electromagnetic wave by dust differ significantly in different channels. By calculating the brightness temperature of sample points in different channels, it was found that the
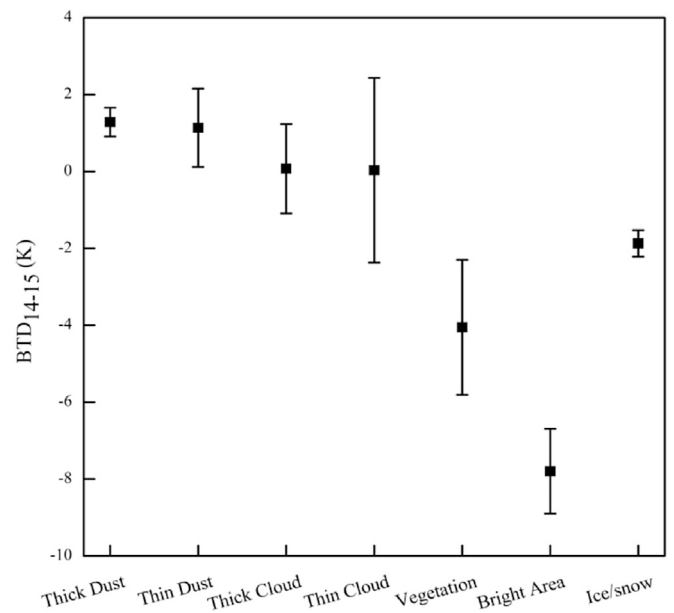
brightness temperature of dust sample points at 3.7 μm (M12) differed greatly from those at 12.013 μm (M16), whereas the brightness temperature of vegetation changed only slightly (Fig. 2-b); thus, vegetation areas can be extracted according to the following condition:

$$BT_{12} - BT_{16} \leq 17.0 \tag{4}$$

where BT_i represents the brightness temperatures of channels i for VIIRS data.

3.2.4. Dust detection

The split window BTD of dust aerosol under different visibility conditions was simulated using the moderate resolution atmospheric transmission (MODTRAN) 4 model, and the results showed that with an increase in visibility, the BTD first decreased and then increased gradually; when the visibility was 0.5 km, the BTD reached the minimum value (Hu et al., 2008). Radiation energy received by a sensor in the mid-wave channel comes from both the dust reflected radiation and the heat radiation emitted by the dust itself, whereas in the thermal channel, it comes mainly from the heat radiation of dust itself. The dust emissivity at 11 μm was lower than that at 12 μm, leading to the negative BTDs between the channels (Han et al., 2013). Therefore, to eliminate the influence of thin clouds on dust monitoring, the split window BTDs of dust and thin clouds in channels 13, 15 and 16 were analysed. Fig. 6 demonstrates the relationships of BTD, and it is clear that thick dusts and thin clouds can be easily distinguished; however, due to the occasional overlapping of the brightness temperatures between thin dust and clouds, the dust is extracted via a piecewise function in this study. The thin clouds and most thin dust areas can be separated via Formula (5), and the thick dusts can be extracted using Formulas (6) and (7) as follows:

$$3.0 < BT_{13} - BT_{15} < 17.0 \ \& \ BT_{15} - BT_{16} \leq -1.5 \tag{5}$$

$$17.0 \leq BT_{13} - BT_{15} < 25.0 \ \& \ BT_{15} - BT_{16} \leq -0.5 \tag{6}$$

$$BT_{13} - BT_{15} \geq 25.0 \tag{7}$$

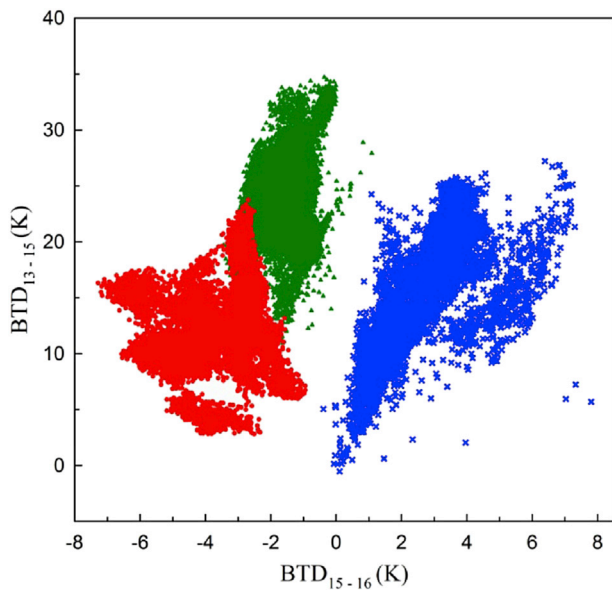where BT_i represents the brightness temperatures of channels i for VIIRS data.

Fig. 6. Scatter plot of the brightness temperature difference between NPP VIIRS channels 13 and 15 versus the VIIRS channels 15 and 16 for thick dust (Green), thin dust (Red) and thin cloud (Blue). (For interpretation of the references to colour in this figure legend, the reader is referred to the web version of this article.)

4. Results and discussion

4.1. Case study

In this study, more than twenty VIIRS images covering the study areas with dust disasters occurred during the period 2012 to 2017 and were collected to perform the dust monitoring experiments using the proposed SDDA algorithm. Meanwhile, the MICAPS ground measured dust data and OMI AI products were selected to validate and compare our detection results. In this paper, three typical dust weather days with different degrees of pollution on April 23, 2014; March 14, 2015, and 5 May, 2016, are selected and showed the spatial distributions of dust storms among different products (Figs. 7–9). The images are true colour composite image (RGB: M5, M4, M3) of VIIRS, the VIIRS dust detection result, the MICAPS ground dust measurement and the OMI AI product result, respectively. In addition, Fig. 10 shows the thick and thin dust storm monitoring results over different areas from 2012 to 2017.

Fig. 7 shows the strong dust monitoring results at for Xinjiang province and Inner Mongolia approximately at 14:30 P.M. on April 23, 2014. The main body of the dust storm area is located above the desert (Taklimakan desert and Kumtag desert). The thick dust storms exist as large differences compared with the background in the image, which is easily monitored. Unlike the thick dust storms, thin dust storms are not obvious and are determined with difficulty via visual interpretation. By ignoring the effect of clouds, the dust monitoring results can better meet the scope of monitoring ground stations. The SDDA algorithm can effectively extract the most thin dust storm areas compared with the true colour composite images. Due to the absence of OMI AI products, only the majority of the monitoring results in the eastern areas was compared. The dust monitoring results showed large agreements in spatial distributions with the OMI AI product.

Fig. 8 shows a typical thick dust storm that occurred at the junction of China and Mongolia, as well as Inner Mongolia, at approximately 13:00 on March 14, 2015. The area is typical of desert and sparse vegetation areas; therefore, it increased the difficulty of determining the scope of the dust by visual interpretation. A thick dust storm can be effectively identified compared with the true colour composite image. In addition, the ground stations marked as dust storm are concentrated mainly in the thick sand dust area. The area is determined to be a dust area via MICAPS data, thus indicating the false negatives for dust over desert areas. Compared with OMI AI products, the dust monitoring results showed
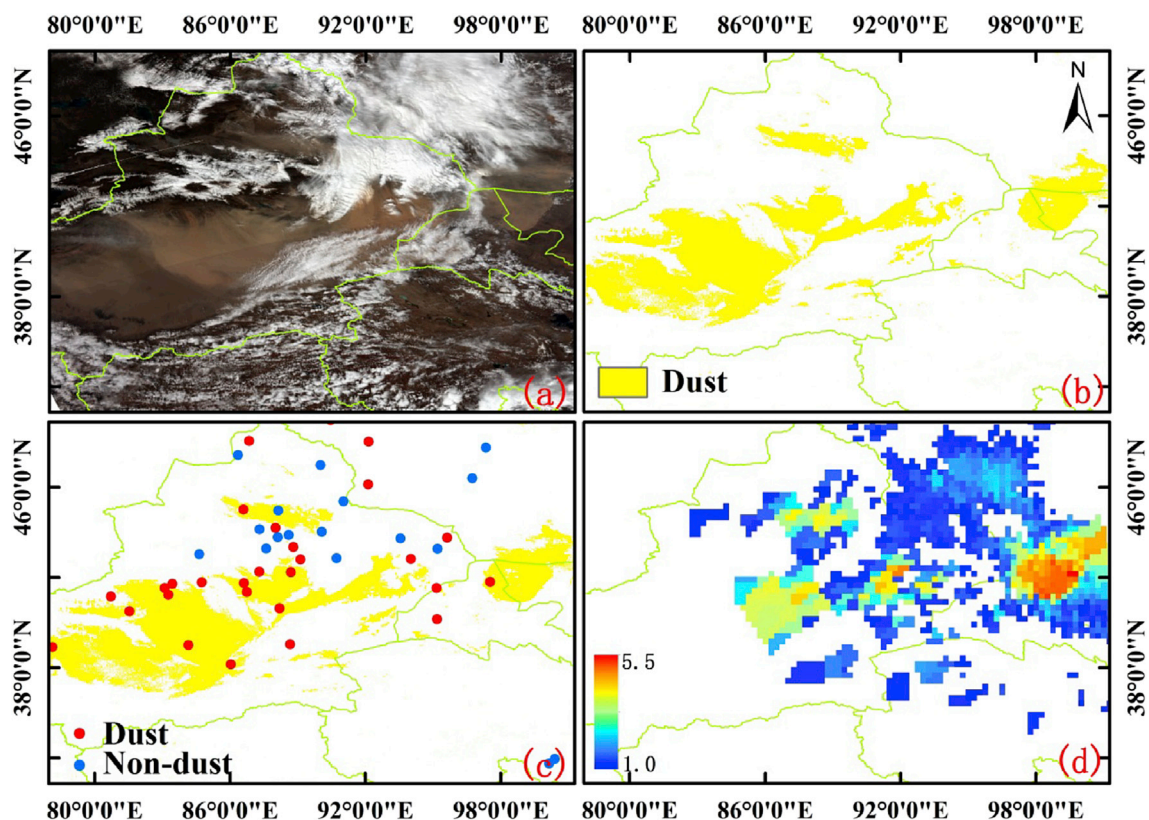

Fig. 7. VIIRS dust detection results b) with an RGB image a), MICAPS Data c), and OMI AI products d) on April 23, 2014.
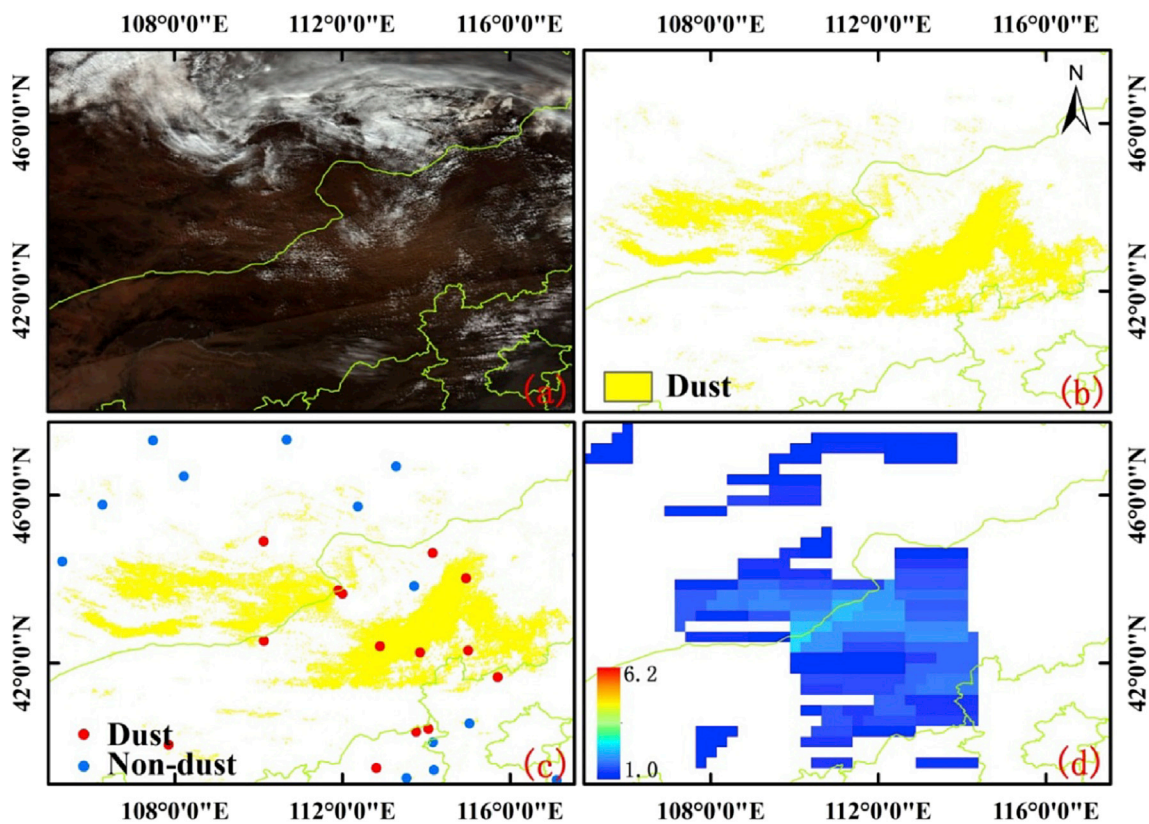
Fig. 8. VIIRS dust detection results b) with an RGB image a), MICAPS Data c), and OMI AI products d) on March 14, 2015.
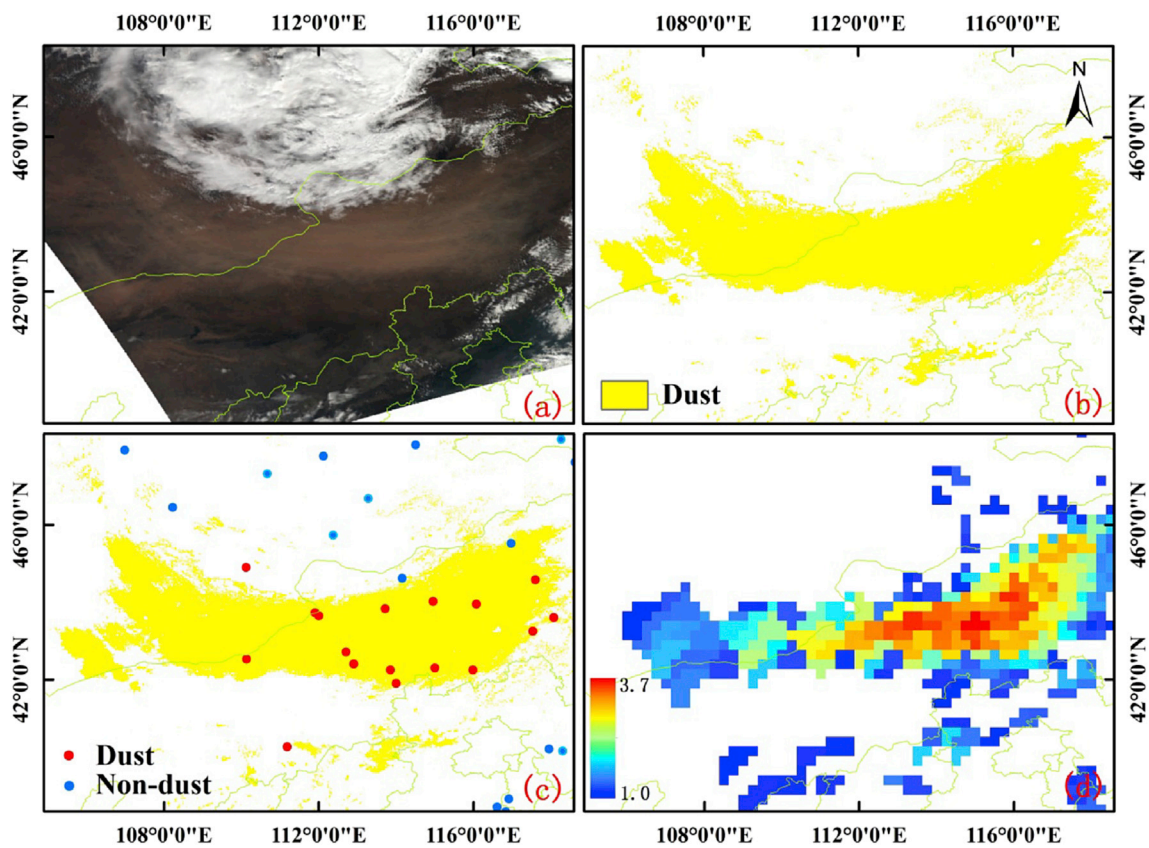
Fig. 9. VIIRS dust detection results b) with an RGB image a), MICAPS Data c) and OMI AI products d) on May, 2016.
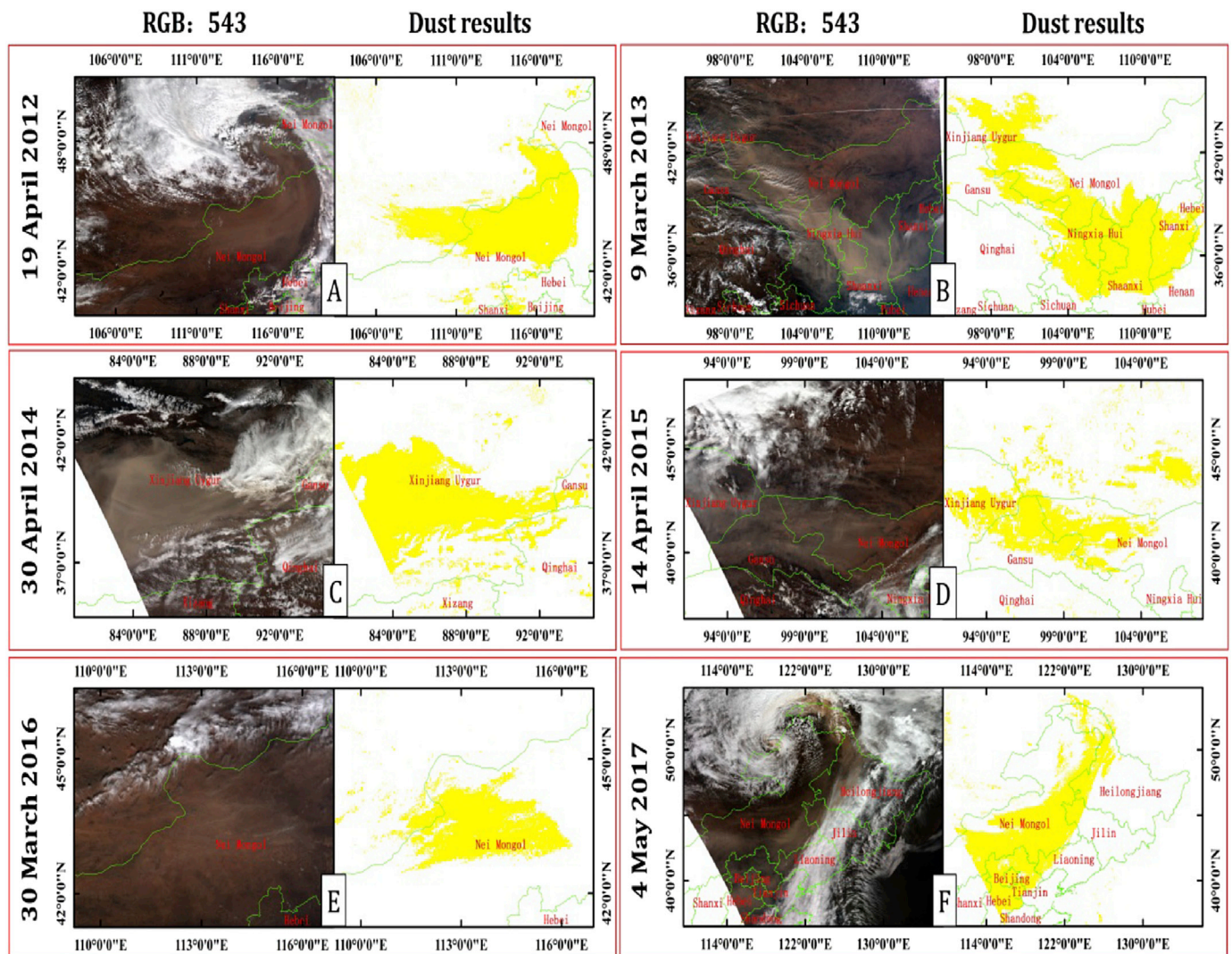
Fig. 10. VIIRS dust storm detection results from 2012 to 2017 in the northern China and Mongolian regions.

high agreement with those in the spatial distributions of dust storms. Validation and comparison indicated that the new proposed SDDA algorithm can better distinguish the dust areas over both bright and dark surfaces.

Fig. 9 shows the strong dust weather that occurred approximately 12:30 on 5 May, 2016, in central Inner Mongolia. The true colour images showed that the dust storm was largely influenced by cyclonic rotation and that the dust source is the boundary of Inner Mongolia and Mongolia, which are thin dust areas. As underlying surface is bare land, it is difficult to distinguish dust areas via visual interpretation. Moreover, ground stations can correctly monitor the dust storms, except in cloud-covered areas. The results showed that the dust edges were in good agreement with the MICAPS ground measurements. In addition to the differences in OMI AI and VIIRS imaging time, the dust detection results were consistent with those of OMI AI products, except for the differences between the dust edge and the dust detection results on the right side of the image. However, it is clear to that the SDDA algorithm can detect most of the dust storms well, with few misses or erroneous phenomena, and that our dust monitoring results are highly consistent with both the MICAPS ground measurements and OMI AI products.

Fig. 10 shows the SDDA dust storm monitoring results for six NPP VIIRS dataset from 2012 to 2017. The left panel provides the true colour composite images, and the right panel shows the corresponding dust detection results. Thick dust exists in large patches with large dust

contents in the image and are easily identified. In contrast, thin dusts are easily affected by the land surface, especially over bright areas. However, most thin dust storms over different surfaces (including vegetation and bright areas) are better detected with the SDDA compared with the true composite images. The verification results show that the new proposed SDDA algorithm is overall robust and can better distinguish the dust areas over both bright and dark surfaces.

4.2. Accuracy evaluation with MICAPS data

To quantitatively evaluate the stability of the algorithm, a large number of dust storm detection results were collected for validation. Here, the MICAPS ground measured data were used as reference data and were matched with the dust detection results. Four evaluation indices, including the Dust-station Correct Rate (DCR), Non-dust-station Correct Error (NCR), Error Rate (ER) and Missing Rate (MR), were selected for accuracy statistics (Sun et al., 2016) as follows:

$$DCR = DSDP \ / \ TNDS \qquad (8)$$

$$NCR = NSNP \ / \ TNNS \qquad (9)$$

$$ER = NSDP \ / \ TNNS \qquad (10)$$

Table 3
Quantitative analysis of dust storms detection results with MICAPS data.

Date	DCR/%	NCR/%	ER/%	MR/%
20140423	77.78	96.30	3.70	22.22
20140427	100.0	95.20	4.80	0.000
20140503	81.50	91.40	8.60	18.50
20150313	94.70	98.30	1.70	5.300
20150314	76.92	95.56	4.44	23.08
20150401	78.10	92.30	7.70	12.90
20160408	75.00	100.00	0.00	25.00
20160416	75.00	90.00	10.0	25.00
20160505	88.90	97.00	3.00	11.10
Average	**83.10**	**95.12**	**4.88**	**16.90**

$$MR = DSNP / TNDS \tag{11}$$

where DSDP is the Dust Station and Dust Pixels and represents both the MICAPS stations and the detection results that are dust storms; NSNP is the Non-dust Station and Non-dust Pixels and represents both the MICAPS stations and detection results that are not dust storms; NSDP is the Non-dust Station and Dust Pixel and represents the MICAPS stations that are not dust storms but the detection results are dust pixels; and DSNP is the Dust Station and Non-dust Pixel and represents the MICAPS stations that are dust storms, but the detection results are not dust pixels. TNDS and TNNS represent the Total Numbers of Dust Stations and Non-dust Stations, respectively. However, the MICAPS data are only available from 2014 to 2016; thus, a total of nine SDDA dust storm results covering the common period 2014–2016 were collected for accuracy validation. The statistical results are shown in Table 3.

Table 3 gives the quantitative evaluation results for NPP VIIRS data which include serious dust storms on different dates from 2014 to 2016. The accuracy evaluation matrix shows that the SDDA algorithm exhibited good detection accuracies with a high average DCR of 83.10% and NCR of 95.12% and an overall low ER and MR of 4.88% and 16.90%, respectively. The overall accuracy is also usually affected by clouds, especially broken clouds and thin clouds over bright surfaces. The validation and comparison results showed that the SDDA algorithm is robust and can better monitor dust storms under different surface and atmospheric conditions.

5. Conclusions

In this paper, a new Simplified Dust Detection Algorithm (SDDA) for Suomi NPP Visible infrared Imaging Radiometer (VIIRS) was studied. First, the areas of dust and non-dust (e.g., thick cloud, thin cloud, bare land, Gobi, vegetation) were selected from different time phase images between 2012 and 2016 to construct the top-of-atmosphere reflectance and brightness temperature training samples. The differences of radiation characteristics between different surface features and dust were analysed by calculating the mean and variance of the samples. Then, the cloud, ice/snow, bright/dark surface masking rules were established based on fixed thresholds among selected reflectance and temperature brightness channels. Finally, the radiation characteristics of the thin cloud and dust in the bright temperature channels were analysed to realize dust detection over the land surface.

To verify the authenticity of the dust detection results, the dust detection results were validated by MICAPS (Meteorological Information Comprehensive Analysis and Process System) dust ground measurements and OMI AI products. Based on the time differences, the dust detection results showed a deviation. However, the overall results show that the dust detection algorithm can effectively realize the automatic detection of thin and thick dusts over both dark and bright surfaces, with a high overall average Dust-station Correct Rate (DCR) of 83.10% and a low Error Rate (ER) of 4.88%. Additionally, the SDDA shows good applicability over the land surfaces in the study area because it is established based on the analysis of a large number of pixel database training

samples. However, in the future, the seasonal changes need to be carefully considered, and the quantitative verification of dust monitoring results needs be improved.

References

Ackerman, S.A., 1989. Using the radiative temperature difference at 3.7 and 11 μm to tract dust outbreaks. Remote Sens. Environ. 27 (2), 129–133.

Ackerman, S.A., 1997. Remote sensing aerosols using satellite infrared observations. J. Geophys. Res. Atmos. 102 (D14), 17069–17079. http://dx.doi.org/10.1029/96JD03066.

Albrecht, B.A., 1989. Aerosols cloud microphysics and fractional cloudiness. Science 245 (4923), 1227–1230.

Amato, T.E., Andrew, K.H., Michael, J.P., 2006. Development of a new over-water advanced very high resolution radiometer dust detection algorithm. Int. J. Remote Sens. 27 (18), 3903–3924. http://dx.doi.org/10.1080/01431160600646359.

Awad, A.M., Mashat, A.W.S., Alamoudi, A.O., Assiri, M.E., 2016. Synoptic study of the seasonal variability of dust cases observed by the TOMS satellite over northern Saudi Arabia. Theor. Appl. Climatol. 124 (3), 1099–1117. http://dx.doi.org/10.1007/s00704-015-1486-y.

Badarinath, K.V.S., Kharol, S.K., Prasad, V.K., Sharma, A.R., Reddi, E.U.B., Kambezidis, H.D., Kaskaoutis, D.G., 2008. Influence of natural and anthropogenic activities on UV Index variations - a study over tropical urban region using ground based observations and satellite data. J. Atmos. Chem. 59 (3), 219–236. http://dx.doi.org/10.1007/s10874-008-9103-4.

Bilal, M., Nichol, J.E., Bleiweiss, M.P., Dubois, D., 2013. A Simplified high resolution MODIS Aerosol Retrieval Algorithm (SARA) for use over mixed surfaces. Remote Sens. Environ. 136 (136), 135–145.

Bilal, M., Nazeer, M., Nichol, J.E., 2017. Validation of MODIS and VIIRS derived aerosol optical depth over complex coastal waters. Atmos. Res. 186, 43–50.

Borgne, P.L., Péré, S., Roquet, H., 2013. Night time detection of Saharan dust using infrared window channels: application to NPP/VIIRS. Remote Sens. Environ. 137 (10), 264–273. http://dx.doi.org/10.1016/j.rse.2013.06.001.

Cao, H., Amiraslanid, F., Liu, J., Zhou, N., 2015. Identification of dust storm source areas in West Asia using multiple environmental datasets. Sci. Total Environ. 502, 224–235. http://dx.doi.org/10.1016/j.scitotenv.2014.09.025.

Chen, B., Zhang, P., Zhang, B.D., Jia, R., Zhang, Z.J., Wang, T.H., Zhou, T., 2014. An overview of passive and active dust detection methods using satellite measurements. J. Meteorol. Res. 28 (6), 1029–1040. http://dx.doi.org/10.1007/s13351-014-4032-4.

Claquin, T., Schulz, M., Balkanski, Y.J., 1999. Modeling the mineralogy of atmospheric dust sources. J. Geophys. Res. Atmos. 104256 (27), 22243–22256.

Di, A., Xue, Y., Yang, X.H., John, L., Guang, J., Mei, L.L., Wang, J.L., She, L., Hu, Y.C., He, X.W., Che, Y.H., Fan, C., 2016. Dust aerosol optical depth retrieval and dust storm detection for Xinjiang region using indian national satellite observations. Remote Sens. 8 (9), 702. http://dx.doi.org/10.3390/rs8090702.

Gharai, B., Jose, S., Mahalakshm, D.V., 2013. Monitoring intense dust storms over the Indian region using satellite data - a case study. Int. J. Remote Sens. 34 (20), 7038–7048. http://dx.doi.org/10.1080/01431161.2013.813655.

Han, L., Tsunekawa, A., Tsubo, M., Zhou, W.Q., 2013. An enhanced dust index for Asian dust detection with MODIS images. Int. J. Remote Sens. 34 (19), 6484–6495. http://dx.doi.org/10.1080/01431161.2013.802055.

Hao, X., Qu, J.J., 2007. Saharan dust storm detection using moderate resolution imaging spectroradiometer thermal infrared bands. J. Appl. Remote Sens. 1 (1), 6656–6659. http://dx.doi.org/10.1117/1.2740039.

Hillger, D., Seaman, C., Liang, C., Miller, S., Lindsey, D., Kopp, T., 2014. Suomi NPP VIIRS imagery evaluation. J. Geophys. Res. Atmos. 119 (11), 6440–6455. http://dx.doi.org/10.1002/2013JD021170.

Hu, X.Q., Lu, N.M., Niu, T., Zhang, P., 2008. Operational retrieval of Asian sand and dust storm from FY-2C geostationary meteorological satellite and its application to real time forecast in Asia. Atmos. Chem. Phys. 8 (6), 1649–1659. http://dx.doi.org/10.5194/acpd-7-8395-2007.

Huang, J.P., Wang, Y.J., Wang, T.H., Yi, Y.H., 2006. Dusty cloud radiative forcing derived from satellite data for middle latitude regions of East Asia. Prog. Nat. Sci.:Mater. Int. 16 (10), 1084–1089.

Jafari, R., Malekian, M., 2015. Comparison and evaluation of dust detection algorithms using MODIS Aqua/Terra Level 1B data and MODIS/OMI dust products in the Middle East. Int. J. Remote Sens. 36 (2), 597–617.

Janugani, S., Jayaram, V., Cabrera, S.D., Rosiles, J.G., Gill, T.E., Rivera, N., 2008. Directional analysis and filtering for dust storm detection in NOAA-AVHRR imagery. SPIE-The Int. Soc. Opt. Eng. 7334 (48) http://dx.doi.org/10.1117/12.820235.

Kaskaoutis, D.G., Kambezidis, H.D., Nastos, P.T., Kosmopoulos, P.G., 2008. Study on an intense dust storm over Greece. Atmos. Environ. 42 (29), 6884–6896.

Kaskaoutis, D.G., Nastos, P.T., Kosmopoulos, P.G., Kambezidis, H.D., Kharol, S.K., Badarinath, K.V.S., 2010. The aura–OMI aerosol index distribution over Greece. Atmos. Res. 98 (1), 28–39. http://dx.doi.org/10.1016/j.atmosres.2010.03.018.

Levelt, P.F., Oord, G.H.J.V.D., Dobber, M.R., Anssi, M., Huib, V., Johan, D.V., Piet, S., Jens, O.V.L., Heikki, S., 2006. The ozone monitoring instrument. IEEE Trans. Geosci. Remote Sens.. 44(5), 1093–1101. DOI: 10.1109/TGRS.2006.872333 · Source: DBLP.

Li, F., Wang, S., Yu, T., Gu, X.F., Zhang, X.Y., Wang, W.H., Ren, S.L., April 2014. 2016. Changes in aerosol optical and micro-physical properties over northeast asia from a severe dust storm in. Remote Sens. 8 (5), 394. http://dx.doi.org/10.3390/rs8050394.

Madhavan, S., Qu, J.J., Hao, X., 2017. Saharan dust detection using multi-sensor satellite measurements. Heliyon 3 (2), e00241. http://dx.doi.org/10.1016/j.heliyon.2017.e00241.

Miller, S.D., 2003. A consolidated technique for enhancing desert dust storms with MODIS. Geophys. Res. Lett. 30 (20), 1–4. http://dx.doi.org/10.1029/2003GL018279.

Moeller, C., 2012. NPP VIIRS M6 Saturation Study Update. University Wisconsin. March 22. http://slideplayer.com/slide/7013116/.

Samadi, M., Boloorani, A.D., 2014. Global dust Detection Index (GDDI); a new remotely sensed methodology for dust storms detection. J. Environ. Health Sci. Eng. 12 (1), 20. http://dx.doi.org/10.1186/2052-336X-12-20.

Sang, S.P., Kim, J., Lee, J., Lee, S., Jeong, S.K., Lin, S.C., Steve, O., 2014. Combined dust detection algorithm by using MODIS infrared channels over East Asia. Remote Sens. Environ.. 141(2), 24–39. DOI: 10.1016/j.rse.2013.09.019.

Sun, L., Wei, J., Bilal, M., Tian, X.P., Jia, C., Guo, Y.M., Mi, X.T., 2015. Aerosol optical depth retrieval over bright areas using Landsat 8 OLI images. Remote Sens. 8 (1), 13.

Sun, L., Wei, J., Wang, J., Mi, X., Guo, Y., Lv, Y., Yang, Y.K., Gan, P., Zhou, X.Y., Jia, C., Tian, X.P., 2016. A universal dynamic threshold cloud detection algorithm (UDTCDA) supported by a prior surface reflectance database. J. Geophys. Res. Atmos. 121 (12), 7172–7196.

Tegen, I., 2003. Modeling the mineral dust aerosol cycle in the climate system. Quat. Sci. Rev. 22, 1821–1834.

Torres, O., Tanskanen, A., Veihelmann, B., Changwoo, A., Remco, B., Pawan, K.B., Pepijn, V., Pieternel, L., 2007. Aerosols and surface UV products from Ozone Monitoring Instrument observations: an overview. J. Geophys. Res. Atmos. 112 (D24), 1–14. http://dx.doi.org/10.1029/2007JD008809.

Wallace, J.M., 2006. Atmospheric Science: an Introductory Survey. Academic Press, Incorporated, Elsevier Australia (Distributor).

Wei, J., Sun, L., 2017. Comparison and evaluation of different MODIS aerosol optical depth products over the Beijing-Tianjin-Hebei region in China. IEEE J. Sel. Top. Appl. Earth Observations Remote Sens. 10 (3), 835–844.

WMO Climate and land degradation, 2005. World Meteorological Organization. Switzerland. http://www.wmo.int/pages/prog/wcp/agm/meetings.php.

Xu, D., Qu, J.J., Niu, S.J., Hao, X.J., 2011. Sand and dust storm detection over desert regions in China with MODIS measurements. Int. J. Remote Sens. 32 (24), 9365–9373. http://dx.doi.org/10.1080/01431161.2011.556679.

Xu, L., Mu, G., Ren, X., Sun, L., Lin, Y.C., Wan, D.J., 2016. Spatial distribution of dust deposition during dust storms in Cele Oasis, on the southern margin of the Tarim Basin. Arid Land Res. Manag. 30 (1), 25–36.

Zhao, C., Chen, S., Leung, L.R., Qian, Y., Kok, J., Zaveri, R., Huang, J., 2013. Uncertainty in modeling dust mass balance and radiative forcing from size parameterization. Atmos. Chem. Phys. 13 (21), 10733–10753.

Zhao, T.X.P., Ackerman, S., Guo, W., 2010. Dust and smoke detection for multi-channel imagers. J. Remote Sens. 2 (10), 2347–2368.

Zheng, X.J., Lu, W.J., Luo, J.N., 2001. Research on the dust storm monitoring using Multi_channel meteorological satellite data. J. Remote Sens. 5 (4), 300–305.

Zhou, C.H., Gong, S.L., Zhang, X.Y., Wang, Y.Q., Niu, T., Liu, H.L., Zhao, T.L., Yang, Y.Q., Hou, Q., 2007. Development and evaluation of an operational SDS forecasting system for East Asia: CUACE/DUST. Atmos. Chem. Phys. 8 (4), 787–798.